Soft Matter

PAPER

View Article Online
View Journal | View Issue

CrossMark click for updates

Cite this: *Soft Matter*, 2016, 12, 7350

Taylor line swimming in microchannels and cubic lattices of obstacles†

Jan L. Münch,[a] Davod Alizadehrad,[ab] Sujin B. Babu[c] and Holger Stark*[a]

Microorganisms naturally move in microstructured fluids. Using the simulation method of multi-particle collision dynamics, we study in two dimensions an undulatory Taylor line swimming in a microchannel and in a cubic lattice of obstacles, which represent simple forms of a microstructured environment. In the microchannel the Taylor line swims at an acute angle along a channel wall with a clearly enhanced swimming speed due to hydrodynamic interactions with the bounding wall. While in a dilute obstacle lattice swimming speed is also enhanced, a dense obstacle lattice gives rise to geometric swimming. This new type of swimming is characterized by a drastically increased swimming speed. Since the Taylor line has to fit into the free space of the obstacle lattice, the swimming speed is close to the phase velocity of the bending wave traveling along the Taylor line. While adjusting its swimming motion within the lattice, the Taylor line chooses a specific swimming direction, which we classify by a lattice vector. When plotting the swimming velocity *versus* the magnitude of the lattice vector, all our data collapse on a single master curve. Finally, we also report more complex trajectories within the obstacle lattice.

Received 7th June 2016,
Accepted 15th July 2016

DOI: 10.1039/c6sm01304j

www.rsc.org/softmatter

Open Access Article. Published on 15 July 2016. Downloaded on 1/23/2026 2:08:07 AM.
This article is licensed under a Creative Commons Attribution 3.0 Unported Licence.

I. Introduction

The motility of microorganisms in their liquid environment is important in various biological processes.[1] Microorganisms move in the low-Reynolds-number regime, where viscous forces dominate over inertia.[2] They have developed various swimming strategies to cope with the strong viscous forces[2] including beating flagellar appendages of sperm cells,[3,4] metachronal waves of collectively moving cilia on the cell surface of a paramecium,[5] rotating helical flagella in *E. coli*,[6–10] and periodic deformations of the whole cell body.[11–13] The first expression for the swimming speed of a simplified flagellar model was given by Taylor in 1951.[14,15] In this model a prescribed bending wave moves along a filament, which we call the Taylor line in the following. A recent study on the Taylor line showed hydrodynamic phase locking of multiple flagella[16] and ref. 17 determined the optimal shape of a large amplitude wave. These insights into biological swimming mechanisms in Newtonian liquids inspired the studies of artificial swimmers in unbound[18,19] as well as bound[20,21] fluids.

Following the seminal experiments of Rothschild in 1963,[22] artificial microchannels have extensively been used to investigate the influence of bounding walls on locomotion.[13,23–36] Hydrodynamic interactions of sperm cells with channel walls[37–42] and with other cells[43] are of special interest in reproductive medicine.

In vivo the motility of protozoa and small eukaryotic organisms is influenced by obstacles in the liquid environment such as cells[44–46] and proteins,[47–51] but also studies with artificially produced posts exist.[11,52,53] Not only the shape of the obstacles is important but they also can make the liquid environment viscoelastic. Examples in nature of biological or medical relevance include microorganisms in soil,[52,53] in blood,[44–46] or in mucus.[54–57] The mucus of the cervix uteri, for example, consists of a dense polymer network. This polymer network induces a hydrodynamic sorting process. Sperm with normal swimming motion are able to pass the network whereas for defective sperm cells the mucus is hardly penetrable.[4] Model swimmers with large-amplitude deformations of their driving filament show speed enhancement in viscoelastic fluids,[58,59] while for small-amplitude deformations viscoelasticity hinders faster swimming.[50,58,60–62] Experiments with *C. elegans* in viscoelastic fluids confirm the prediction of slower swimming.[49,63]

In 1979 L. Turner and H. C. Berg suggested that the geometric constraints of polymer networks in viscoelastic fluids can drastically enhance the swimming speed of microorganisms.[48] Based on experimental observations with helical bacteria they formulated the following picture. When rotating about their helical axis, bacteria with helical shape move through a polymeric liquid like through a quasi-rigid medium and similar to a corkscrew driven into cork. So, in the ideal case, after each full rotation the bacterium would proceed by

[a] *Institut für Theoretische Physik, Technische Universität Berlin, Hardenbergstr. 36, D-10623 Berlin, Germany. E-mail: Holger.Stark@tu-berlin.de; Web: http://www.itp.tu-berlin.de/stark*
[b] *Forschungszentrum Jülich, Wilhelm-Johnen-Straße, D-52425 Jülich, Germany*
[c] *Department of Physics, Indian Institute of Technology Delhi, Hauz Khas, New Delhi-110016, India*

† Electronic supplementary information (ESI) available. See DOI: 10.1039/c6sm01304j

This journal is © The Royal Society of Chemistry 2016

Open Access Article. Published on 15 July 2016. Downloaded on 1/23/2026 2:08:07 AM.
This article is licensed under a Creative Commons Attribution 3.0 Unported Licence.

one full pitch length. In this paper we will investigate another type of this geometrical swimming by studying the Taylor line in a cubic lattice of obstacles.

A typical example of obstacles in nature is erythrocytes or red blood cells. The African trypanosome, the causative agent of sleeping sickness, swims faster in the crowded environment of blood and thereby removes surface-bound antibodies with the help of hydrodynamic drag forces.[46] In this way, the parasite evades the immune response of its host. The motility of the African trypanosome in a Newtonian liquid was investigated in bulk fluid by computer modeling[64–66] and in Poiseuille flow.[34] Blood is a complex viscoelastic liquid containing a large amount of cellular components, which gives blood a non-Newtonian character. Its viscosity depends on the volume fraction of erythrocytes (hematocrit), shear rate, and temperature.[67,68] In order to understand the geometrical constraints of erythrocytes for the motility of the trypanosome or how other obstacles influence the swimming of sporozoites or *C. elegans*, more controlled experiments were conducted. They use either suspended colloids[63,69] or fabricated lattices of posts.[11,52,53,70,71]

In lab-on-chip devices obstacle lattices are used to separate trypanosomes from erythrocytes with the idea to diagnose the sleeping sickness in an early stage.[72] Trypanosomes swimming in these lattices show a motility much more comparable to their *in vivo* motility due to interactions with the obstacles.[11] Similarly, Park *et al.* found that *C. elegans*, a worm-like microorganism, swims up to ten times faster in an obstacle lattice compared to its swimming speed in bulk fluid.[52] The speed-up depended on the lattice spacing. A combined experimental and numerical study by Majmudar *et al.* on an undulatory swimmer such as *C. elegans* showed that most of the characteristics of this new type of swimming in an array of micro-pillars can be explained by a mechanical model for the swimmer.[53] It does not need any biological sensing or behavior.

In this paper we present a detailed hydrodynamic study of an undulatory Taylor line (a one-dimensional object) swimming in a two-dimensional microchannel and in a two-dimensional cubic lattice of obstacles. We use the method of multi-particle collision dynamics for simulating the hydrodynamic flow fields.[73] In the microchannel the Taylor line swims at an acute angle along a channel wall with a clearly enhanced swimming speed. In a dilute obstacle lattice swimming speed is also enhanced due to hydrodynamic interactions with the obstacles similar to a study by Leshansky.[74] Moving the obstacles closer together (dense obstacle lattice), the undulatory Taylor line has to fit into the free space of the obstacle lattice, where it performs geometric swimming. Here, the swimming speed is close to the wave velocity of the bending wave traveling along the Taylor line. In this regime, we classify the possible swimming directions by lattice vectors. When plotting the ratio of swimming and wave velocity *versus* the magnitude of the lattice vector (effective lattice constant), all our data collapse on a single master curve. This demonstrates the regime of geometric swimming. We also illustrate more complex trajectories. With our study, we contribute to the understanding of undulatory biological microswimmers, such as the African trypanosome or *C. elegans* in complex environments.

The article is structured as follows. In Section II we introduce our computational methods including the method of multi-particle collision dynamics and the implementation of the Taylor line. In Section III we calibrate the parameters of the Taylor-line model by studying its swimming motion in the bulk fluid. In Sections IV and V we review the respective results for swimming in the microchannel and in the obstacle lattice. Section VI closes with a summary and conclusions.

II. Computational methods

A. Multi-particle collision dynamics

We employ the method of multi-particle collision dynamics (MPCD) to simulate the Taylor line in its two-dimensional fluid environment.[75–77] This method has been applied to various physical problems reviewed in ref. 73 and 78. Of particular interest to the present work on MPCD one can implement no-slip boundary conditions and therefore reproduce flow fields in channels,[79,80] around circular[79,81] or cubic cylinders,[81] and around passive spheres[82] in good agreement with analytical formulae. Furthermore, microswimmers moving by surface deformations can be simulated by coupling them to the surrounding fluid at low Reynolds numbers.[38,64–66] Recent theoretical studies in two dimensions simulate a moving fish,[83] the sedimentation of erythrocytes,[84] and a binary colloidal suspension demixing under Poiseuille flow.[85]

MPCD uses point particles of mass m_0 as coarse-grained fluid particles. Their dynamics consists of a ballistic streaming and a collision step, which locally conserves momentum. Therefore, the resulting flow field satisfies the Navier–Stokes equations but also inherently includes thermal fluctuations.[73]

In the streaming step the positions $\vec{r}_i$ of all fluid particles are updated according to

$$\vec{r}_i(t + \Delta t_c) = \vec{r}_i(t) + \vec{v}_i(t)\Delta t_c, \quad (1)$$

where $\vec{v}_i$ is the particle velocity and Δt_c the MPCD time step between collisions.[80]

After each streaming step the fluid particles are sorted into quadratic collision cells of linear dimension a_0, so that on average each cell contains $N = 10$ particles with total mass $M = Nm_0 = 10$. In each cell we redistribute the particles' velocities following a collision rule, for which we choose the Anderson thermostat with additional angular momentum conservation.[80] At first we calculate the total momentum, $\vec{P}_{\text{cell}} = m_0 \sum_{i\in\text{cell}} \vec{v}_i$, of each collision cell. Then, we assign to each velocity component of a particle relative to the mean velocity $\vec{P}_{\text{cell}}/M$ a random component $v_{i,\text{rand}}$ from a Gaussian distribution with variance k_BT/m_0. Here, T is the temperature and k_B the Boltzmann constant. Using the mean random momentum $\vec{P}_{\text{rand}} = m_0 \sum_{i\in\text{cell}} \vec{v}_{i,\text{rand}}$ of each cell, we determine the new particle velocities after the collision:

$$\vec{v}^{\,C}_{i,\text{new}} = \frac{\vec{P}_{\text{cell}}}{M} + \vec{v}_{i,\text{rand}} - \frac{\vec{P}_{\text{rand}}(t)}{M}. \quad (2)$$

Open Access Article. Published on 15 July 2016. Downloaded on 1/23/2026 2:08:07 AM.
This article is licensed under a Creative Commons Attribution 3.0 Unported Licence.

This collision rule conserves linear momentum but not angular momentum.[73] To keep the latter constant, we note that during the collision step the fluid particles have fixed distances. Therefore, one can apply a rigid body rotation, $\Delta\vec{\omega} \times \vec{r}_i$, to replace the new velocities $\vec{v}^{\mathrm{C}}_{i,\mathrm{new}}$ by

$$\vec{v}_{i,\mathrm{new}} = \vec{v}^{\mathrm{C}}_{i,\mathrm{new}} - \Delta\vec{\omega} \times \vec{r}_i. \quad (3)$$

Here, the angular velocity is

$$\Delta\vec{\omega} = m_0 \Theta^{-1} \sum_{i\in\mathrm{cell}} \vec{r}_i \times \left(\vec{v}_{i,\mathrm{rand}} - \vec{v}_i\right), \quad (4)$$

where $\Theta = m_0 \sum_{i\in\mathrm{cell}} |\vec{r}_i|^2$ is the moment of inertia of the particles in the cell. This rule restores angular momentum conservation keeping linear momentum constant. By definition, the collision rule based on the Anderson thermostat also keeps the temperature constant. To restore Galilean invariance and the molecular chaos assumption, we always apply a random grid shift when defining the collision cells and take the shift from the interval $[0,a_0]$.[86,87]

In the following, we will measure quantities in typical MPCD units. We will use the linear dimension of the collision cell a_0 as a unit for length, energies are measured in units of $k_{\mathrm{B}}T = 1$, and mass in units of m_0. Then the time unit becomes $\tau_0 = a_0\sqrt{m_0/k_{\mathrm{B}}T}$.[82] In this unit, our time step between collisions is always chosen as $\Delta t_{\mathrm{c}} = 0.01$.

Transport coefficients of the MPCD fluid in two and three dimensions can be found in ref. 77. In particular, in MPCD units we obtain a shear viscosity of $\eta \approx 36$ for the parameters in our simulations, in agreement with ref. 88. To calculate the Reynolds number $\mathrm{Re} = \rho v 2A/\eta$, we use $\rho = 10$ (as introduced before), A is the amplitude of the undulation of the Taylor line, and $v = 4A\omega/2\pi$ estimates the velocity of the constituent beads, when moving up and down. The highest value in our simulations amounts to $v = 0.06$ in MPCD units, so that we work at Reynolds numbers below Re = 0.11. These are typical values used in two- and three-dimensional MPCD simulations for the low-Reynolds-number regime.[43,88]

All particle-based solvers of the Navier–Stokes equations describe, in principle, compressible fluids, which are characterized by the Mach number $\mathrm{Ma} = v/v_{\mathrm{sound}}$. Here $v_{\mathrm{sound}} = \sqrt{1+2/f}$ is the sound velocity of the MPCD fluid in MPCD units and f is the spatial dimension. Since the compressibility scales with Ma^2, the accepted regime in MPCD simulations for neglecting compressibility is $\mathrm{Ma} < 0.1$.[81–83] Using $v_{\mathrm{sound}} = \sqrt{2}$ and the maximal value $v = 0.06$ from above, we arrive at the maximal value $\mathrm{Ma} \approx 0.05$, well in the regime where incompressibility can safely be assumed.

B. No-slip boundary condition: bounce-back rule and virtual particles

At bounding walls fluid flow obeys the no-slip boundary condition. To implement it within the MPCD method, we let the effective fluid particles interact with channel walls or obstacles using the bounce-back rule,[81] see Fig. 1. When a fluid particle moves into an obstacle or a channel wall during the streaming step (position B), we invert the velocity $\vec{v}_i' = -\vec{v}_i$ and let the particle stream to position C during half the collision time:

$$\vec{r}_i(t + \Delta t_{\mathrm{c}}/2) = \vec{r}_i(t) + \vec{v}_i'(t)\Delta t_{\mathrm{c}}/2. \quad (5)$$

Then, we move this particle to the closest spot on the obstacle surface or channel wall (position D) and let it stream with the reversed velocity during half the collision time to position E.[89]

In addition, the no-slip boundary condition is improved using virtual particles inside a channel wall or an obstacle, see Fig. 2. We uniformly distribute virtual particles (red dots in Fig. 2) in the areas of the collision cells, which extend into the channel wall or obstacles. The velocity components are chosen from a Gaussian distribution with variance $k_{\mathrm{B}}T/m_0$. The virtual particles also take part in the collision step. So, close to bounding walls one has the same average number of particles in a collision cell as in the bulk. Both rules together implement the no-slip boundary condition at a bounding surface in good approximation.[80,81]

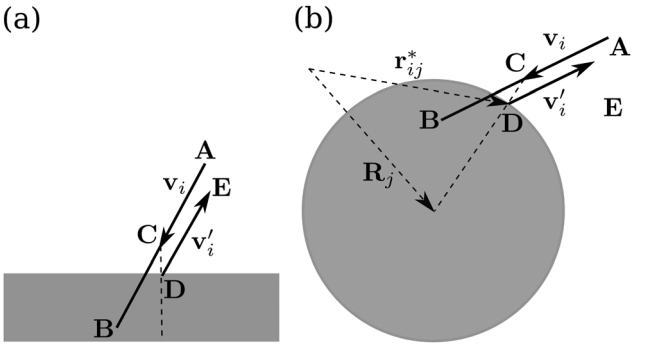

Fig. 1 Sketch of the bounce-back rule at (a) a channel wall and (b) an obstacle. Particle positions during implementation of the rule are denoted by capital letters and explained in the main text. The velocities before and after the bounce are denoted by $\vec{v}_i$ and $\vec{v}_i' = -\vec{v}_i$, respectively. [Reproduced with permission from the PhD thesis of A. Zöttl (https://depositonce.tu-berlin.de/handle/11303/4329).]

C. A discrete model of the Taylor line

The Taylor line propels itself by running a sinusoidal bending wave along its contour line. Fig. 3(a) shows how we discretize the Taylor line by a bead-spring chain with N beads each of

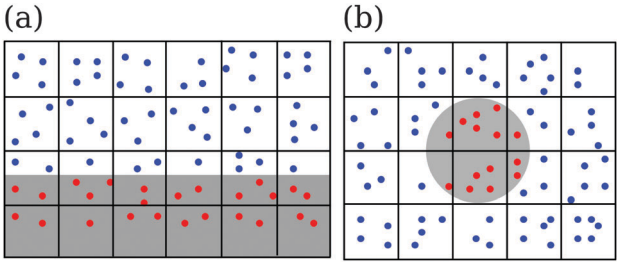

Fig. 2 Coarse-grained fluid particles (blue) and virtual particles (red) close to (a) a channel wall and (b) an obstacle, which are represented by gray areas. Both figures show the lattice of collision cells. The fluid particles cannot penetrate into the gray areas.

This journal is © The Royal Society of Chemistry 2016

Open Access Article. Published on 15 July 2016. Downloaded on 1/23/2026 2:08:07 AM.
This article is licensed under a Creative Commons Attribution 3.0 Unported Licence.

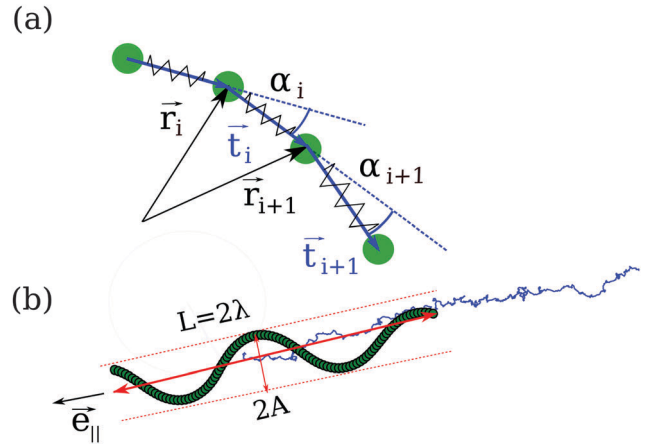

Fig. 3 (a) The Taylor line is modeled as a bead-spring chain, where $\vec{r}_i$ gives the bead position. The tangential vector $\vec{t}_i = \vec{r}_{i+1} - \vec{r}_i$ connects two neighboring beads and is not normalized to one. The angles α_i between the tangential vectors are used to define the sinusoidal bending wave running along the Taylor line. (b) Snapshot of the Taylor line, which swims along the unit vector $\vec{e}_\parallel$ in a bulk fluid with superimposed thermal diffusion. The blue line represents the center-of-mass trajectory. The end-to-end distance of the Taylor line or its length along $\vec{e}_\parallel$ is $L = 2\lambda$, where λ is the wavelength of the bending wave along $\vec{e}_\parallel$ and A its amplitude.

mass $m = 10m_0$. The beads at positions $\vec{r}_i$ interact with each other by a spring and a bending potential. The spring potential implements Hooke's law between nearest neighbors,[19]

$$V_{\mathrm{H}} = \frac{D}{2}\sum_{i=1}^{N-1}\left(|\vec{t}_i| - l_0\right)^2. \tag{6}$$

Here $l_0 = 1/2a_0$ is the equilibrium distance between the beads and $|\vec{t}_i| = |\vec{r}_{i+1} - \vec{r}_i|$ the actual distance, where $\vec{t}_i$ denotes the tangent vectors. The contour length of the bead-spring chain,

$$L_{\mathrm{c}} = \sum_{i=1}^{N-1}|\vec{t}_i| \approx (N-1)l_0 = (N-1)a_0/2, \tag{7}$$

is approximately constant. We choose a large spring constant $D = 10^6$ to ensure that deviations from the equilibrium distance l_0 between the beads are smaller than $0.002l_0$. Finally, the spring force acting on bead i is

$$\vec{F}_i^{\mathrm{H}} = -\vec{\nabla}_i V_{\mathrm{H}} = -D(l_i - l_0)\vec{t}_i + D(l_{i+1} - l_0)\vec{t}_{i+1}. \tag{8}$$

The bending potential creates a sinusoidal bending wave that runs along the Taylor line. It was also used in two-dimensional studies of swimming sperm cells[43] and in simulations of the African trypanosome.[64,65] The bending potential has the form:

$$V_{\mathrm{B}} = \frac{\kappa}{2}\sum_{i=1}^{N-1}\left[\vec{t}_{i+1} - R(\alpha_i)\vec{t}_i\right]^2, \tag{9}$$

where $\kappa = pk_{\mathrm{B}}T$ is the bending rigidity and p the persistence length.[90] The rotation matrix $R(\alpha)$ rotates the tangential vector by an angle α about the normal of the plane, so the equilibrium shape of the Taylor line is not straight but bent. For the rotation angle at bead n we choose $\alpha_n = l_0 c(n,t)$, where the equilibrium curvature,

$$c(n,t) = b\sin[\phi(t,n)] = b\sin[2\pi(\nu t + nl_0/\lambda_{\mathrm{c}})], \tag{10}$$

is a function of the position of bead n on the Taylor line ($n \in \{1,N\}$) and time t. It creates the sinusoidal bending wave running along the Taylor line with wavelength λ_{c} (measured along the contour) and an amplitude A controlled by the parameter b. Unless stated otherwise, we choose the ratio of persistence to contour length as $p/L_{\mathrm{c}} = 5 \times 10^3$ to ensure that bending forces are much stronger than thermal forces, in order to induce directed swimming.[43] This is investigated in more detail in Section III.

Active biological filaments such as flagella in sperm cells are actuated by internal motors. They apply forces on the filament and thereby generate the bending waves travelling along the flagellum. This mechanism is implemented by the special form of the bending potential of eqn (9), which locally prescribes the curvature of the Taylor line as given in eqn (10). However, since the bending potential allows for deviations from the prescribed curvature, the Taylor line can react on external forces, as any real active filament does, and thereby change its shape. Keeping the shape of the travelling wave fixed would not take this effect into account. Thus our model addresses undulatory swimmers such as the sperm cell, the African trypanosome, or the worm *C. elegans* as mentioned in the introduction.

From the bending potential (9) we derive a bending force acting on bead j:

$$\begin{aligned}\vec{F}_j^{\mathrm{B}} &= -\vec{\nabla}_j V_{\mathrm{B}} = \kappa\big(\left[R(\alpha_{j-2})\vec{t}_{j-2} - \vec{t}_{j-1}\right] \\ &\quad + \left[\vec{t}_j - \vec{t}_{j-1} + R^{\mathrm{T}}(\alpha_{j-1})\vec{t}_j - R(\alpha_{j-1})\vec{t}_{j-1}\right] \\ &\quad + \left[\vec{t}_j - R^{\mathrm{T}}(\alpha_j)\vec{t}_{j+1}\right]\big)\end{aligned} \tag{11}$$

where $R^{\mathrm{T}}(\alpha_j)$ is the transposed matrix. Then, the total force $\vec{F}_i = \vec{F}_i^{\mathrm{H}} + \vec{F}_i^{\mathrm{B}}$ determines the dynamics of the Taylor line. In our simulations we update the positions of the beads during the streaming step using the velocity Verlet algorithm with time step $\delta t = 0.01\Delta t_{\mathrm{c}}$.[65] In addition, the beads with mass $m = 10m_0$ participate in the collision step and the components of their random velocities $\vec{v}_{i,\mathrm{rand}}$ are chosen from a Gaussian distribution with $k_{\mathrm{B}}T/10m_0$. The beads thereby interact with the fluid particles which ultimately couples the Taylor line to the fluid environment. Note, since the beads of the Taylor line have a different mass than the fluid particles, in all the formulas of Section II.A one has to replace $m_0\sum_{i\in\mathrm{cell}}\ldots$ by $\sum_{i\in\mathrm{cell}} m_i\ldots$, where m_i is the mass of either the fluid particles or the Taylor line beads. The latter also interact with channel walls or obstacles by the bounce-forward rule, which is very similar to the bounce-back rule used for the fluid particles. Upon streaming into an obstacle or wall, we place the particle onto position D; see Fig. 1. However, in contrast to the bounce-back rule, only the velocity component of the bead orthogonal to the surface is inverted. This ensures that the Taylor line can slip along a surface.

Open Access Article. Published on 15 July 2016. Downloaded on 1/23/2026 2:08:07 AM.
This article is licensed under a Creative Commons Attribution 3.0 Unported Licence.

We introduce the normalized end-to-end vector of the Taylor line,

$$\vec{e}_{\parallel} = \frac{1}{\left|\sum_{i=1}^{N-1} \vec{t}_i\right|} \sum_{i=1}^{N-1} \vec{t}_i, \tag{12}$$

to quantify the mean swimming direction and denote the end-to-end distance by L. Unless mentioned otherwise, we always fit two complete bending wave trains onto the Taylor line, meaning $L = 2\lambda$, where λ is the wavelength measured along $\vec{e}_{\parallel}$ [see Fig. 3(b)]. Note that λ is different from the wavelength λ_c along the contour introduced in eqn (10). In the following, we will vary the amplitude A of the bending wave keeping the end-to-end distance with $L = 2\lambda$ fixed. Therefore, we always have to adjust the contour length of the Taylor line by adding or removing some beads. Typically, we use Taylor lines with $L = 42a_0$ and the number of beads ranges from $N = 88$ to 125.

III. Taylor line in the bulk fluid

In the following we discuss the swimming velocity of the Taylor line as a function of the dimensionless persistence length p/L_c. Thermal fluctuations noticeably bend an elastic line on lengths comparable to the persistence length. So, in our case the Taylor line should have the form of a sine wave when p is much larger than its contour length L_c. In addition, the Taylor line performs translational and rotational Brownian motion as thermal fluctuations are inherently present in the MPCD fluid. All this is visible in Fig. 4. In case (a) with $p/L_c = 1$ the Taylor line is too floppy and the bending wave cannot develop. Only thermal motion of the center of mass occurs (blue line), reminiscent of a Brownian particle. In case (b) with $p/L_c = 10$ the bending wave is clearly visible, although still distorted by thermal fluctuations, and the Taylor line exhibits persistent motion. The Taylor line has a fully undistorted, sinusoidal contour in case (c) at $p/L_c = 500$. The trajectory of the center of mass shows directed swimming superimposed by Brownian motion. The total displacement over a complete simulation run is larger compared to (b) and the Taylor line has reached its maximum propulsion speed.

To discuss directed swimming more quantitatively, we introduce the swimming velocity $v_{\parallel} = \mathrm{d}\vec{r}\cdot\vec{e}_{\parallel}/\Delta t$, where we project the center-of-mass displacement $\mathrm{d}\vec{r}$ during time Δt onto the mean direction of the Taylor line defined in eqn (12) and indicated in Fig. 3(b). We then define the stroke efficiency

$$S = \frac{\langle v_{\parallel}\rangle}{c} = \frac{\langle v_{\parallel}\rangle}{\lambda\nu}. \tag{13}$$

It compares the mean swimming speed, averaged over the whole swimming trajectory, with the phase velocity c, at which the bending wave travels along the Taylor line. Then, $S = 1$ indicates optimal swimming of the Taylor line. In three dimensions this situation is similar to a corkscrew screwed into the cork. It moves at a speed that equals the phase velocity of the helical wave traveling along the rotating corkscrew.

In Fig. 5 we plot the stroke efficiency S *versus* persistence length p/L_c. For $p = L_c$ the stroke efficiency is approximately zero as already observed from the trajectory (a) in Fig. 4. The efficiency S increases nearly linearly in $\log(p/L_c)$ until at *ca.* $p/L_c = 10^2$ it reaches a plateau value. A linear fit gives the plateau value $S_0 = 0.098$ typical for low Reynolds number swimmers. For example, for *C. elegans* studied in ref. 52 we estimate $S = 0.12$. In the following we always use the persistence length $p/L_c = 5 \times 10^3$ to be on the safe side.

Within resistive force theory, one derives for the swimming speed of the Taylor line in the limit of $A \ll \lambda$:

$$\langle v_{\parallel}\rangle = \frac{\xi_{\perp} - \xi_{\parallel}}{2\xi_{\parallel}} \omega k A^2, \tag{14}$$

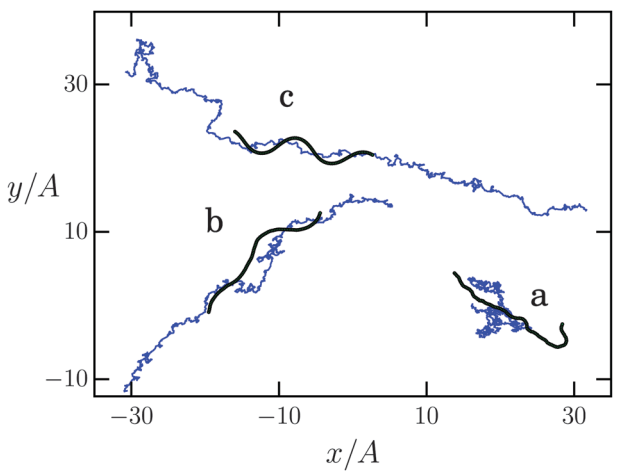

Fig. 4 Taylor line (chain of green dots) swimming and diffusing in a bulk fluid at different persistence lengths normalized by the chain length: (a) $p/L_c = 1$, (b) $p/L_c = 10$, and (c) $p/L_c = 500$. The blue curve represents the center-of-mass trajectory and the chain of green dots shows a typical snapshot. The different trajectories are discussed in the main text.

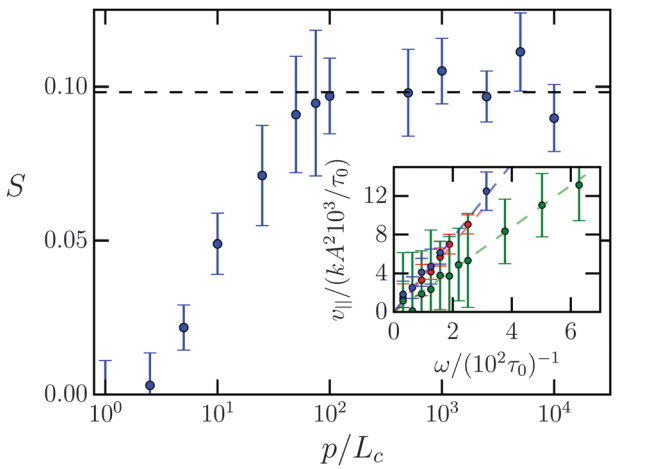

Fig. 5 Stroke efficiency S *versus* dimensionless persistence length p/L_c of the Taylor line. The wave frequency is $\nu = 0.003/\tau_0$ and the amplitude to wavelength ratio is $A/\lambda = 0.14$. The error bar shows the standard deviation of a time average over a simulation period of $3000/\tau_0$. The dashed line is a linear fit of the last 8 data points. The inset shows the swimming velocity $\langle v_{\parallel}\rangle$ in units of kA^2/τ_0 as a function of $\omega\tau_0$ for different values of A/λ. Green: $A/\lambda = 0.04$, blue: $A/\lambda = 0.1$, red: $A/\lambda = 0.14$. The dashed lines are linear fits.

This journal is © The Royal Society of Chemistry 2016

Open Access Article. Published on 15 July 2016. Downloaded on 1/23/2026 2:08:07 AM.
This article is licensed under a Creative Commons Attribution 3.0 Unported Licence.

with the wave number $k = 2\pi/\lambda$ and angular frequency $\omega = 2\pi\nu$. The parameters $\xi_\perp$ and $\xi_\parallel$ are the respective local friction coefficients per unit length for motion perpendicular and parallel to the local tangent.[1] Originally, Taylor used $\xi_\perp = 2\xi_\parallel$ valid for an infinitely long filament. We are able to reproduce the linear relationship between swimming speed $\langle v_\parallel \rangle$ and ω in our simulations (see inset of Fig. 5). Whereas $A/\lambda = 0.1$ (blue) and 0.14 (red) confirm the expected scaling with kA^2, the straight line for $A = 0.04\lambda = 0.9a_0$ deviates from it, possibly because the amplitude is too small to be correctly resolved in the MPCD simulations. Finally, note that we chose ω sufficiently low for all data presented in this article, so that the MPCD fluid was in the regime, where compressibility could be neglected.

IV. Taylor line in a microchannel

In the following we present our simulation data of the Taylor line swimming in a microchannel and discuss it in detail.

A. Swimming on a stable trajectory and under an acute angle at the channel wall

In Fig. 6(a) we show ten center-of-mass trajectories of identical Taylor lines in a wide microchannel with width $d/A = 27.7$. They all start in the middle of the channel and always swim in the negative x direction towards one of the channel walls. After an axial swimming distance of $80A$, 92% of all our simulated Taylor lines have reached one of the channel walls (not all of the trajectories are shown here). We observe that in a very narrow channel with width $d/A = 3.07$, the swimming trajectory is not stable and the Taylor line switches from one wall to the other. However, already at $d/A = 3.75$ it stays at one channel wall. This occurs even though the walls are not further apart than four amplitudes. Stable swimming trajectories at channel walls have been observed in experiments and simulations of sperm cells and *E. coli*.[22,23,38]

Fig. 6(b) shows that the Taylor line swims at an acute tilt angle along the channel wall. Earlier simulations of swimming sperm cells have attributed the attraction to the wall to a pusher-like flow field, which drags fluid in at the sides of the swimmer.[38] Thereby, the sperm cells are hydrodynamically attracted by the wall. Additional flow at the free end of the flagellum pushes the tail of the sperm cell up. In Fig. 6(c) we confirm this picture. Below the wave crests fluid is strongly pulled towards the Taylor line, while fluid flow towards the wall below the wave troughs is much weaker. Hence, the Taylor line is attracted to the wall. In addition, fluid flow towards the wave crest at the front is stronger compared to the second wave crest, which obviously tilts the Taylor line as Fig. 6(b) demonstrates.

In order to investigate the tilt angle ϕ at the channel walls in more detail, in Fig. 7 we plot ϕ *versus* channel width for several amplitude-to-wavelength ratios A/λ. Each curve except for the smallest amplitude A starts with a small region of the channel width $d/A \in [2,3]$, where the tilt angle is *ca.* 0.01π and hardly depends on d/A. Then, at the width $d/A \approx 3$ the tilt angle

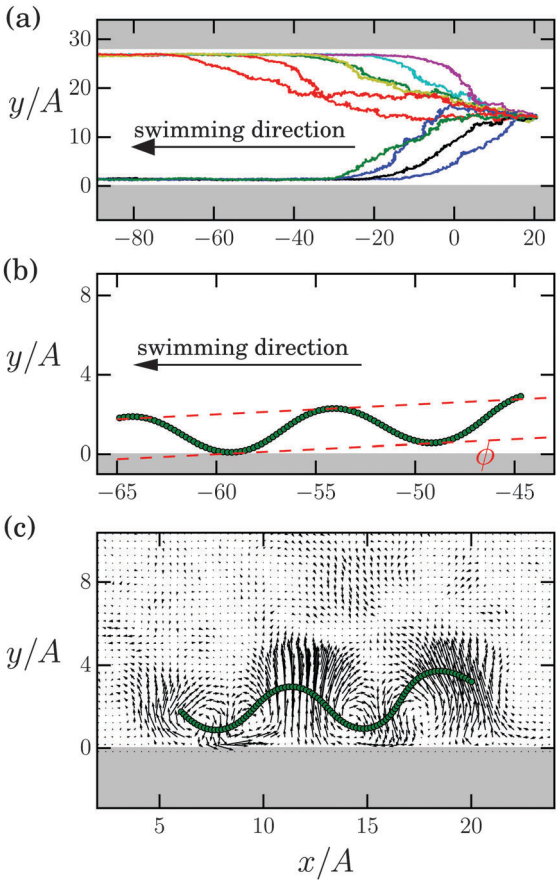

Fig. 6 Taylor lines swim along the walls of a microchannel (gray areas). (a) Ten trajectories of the center of mass start in the middle and reach one of the walls. Parameters are the channel width $d/A = 27.7$, the wave amplitude $A/\lambda = 0.1$, and the wavelength $\lambda = 22.59a_0$. (b) Close-up: the Taylor line swims under an acute tilt angle ϕ along a channel wall. (c) Close-up: flow field initiated by the Taylor line when swimming along the channel wall. Note, amplitude and wavelength of the Taylor lines in (b) and (c) differ since we used different parameter sets.

increases and ultimately reaches a plateau value at $d/A \approx 8$ meaning that the Taylor line does not interact with the other channel wall at widths $d/A \gtrsim 8$. The inset plots the plateau or maximum tilt angle $\phi_{\max}$ *versus* A^2/λ^2. It is determined as the average of all tilt angles for $d/A \gtrsim 8$. The maximum tilt angle $\phi_{\max}$ needs to be an even function in A since $-A$ only introduces a phase shift of π in the bending wave, which does not change the steady state of the Taylor line. Indeed, we can fit our data by

$$\phi(A/\lambda) = \phi_2 \frac{A^2}{\lambda^2} + \phi_0, \tag{15}$$

where $\phi_2 = 1.944$ and $\phi_0 = 0.046$ are fit parameters.

B. Speed enhancement at the channel wall

The swimming speed $\langle v_W \rangle$ of the Taylor line along the channel wall is enhanced compared to the bulk value $\langle v_\parallel \rangle$ and strongly depends on the channel width. To discuss this effect thoroughly, we define a speed enhancement factor

$$\gamma = \langle v_W \rangle / \langle v_\parallel \rangle, \tag{16}$$

Open Access Article. Published on 15 July 2016. Downloaded on 1/23/2026 2:08:07 AM.
This article is licensed under a Creative Commons Attribution 3.0 Unported Licence.

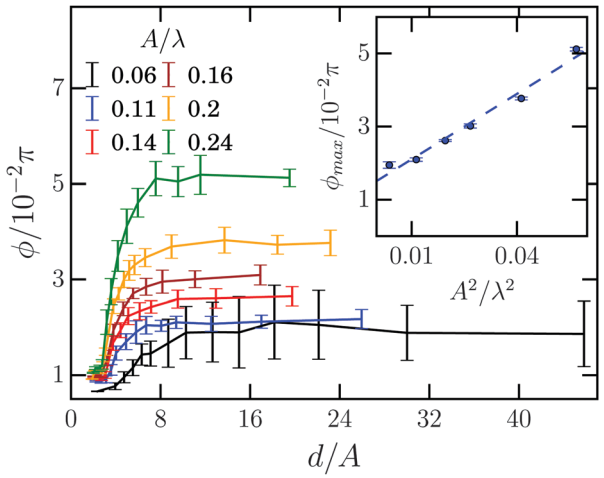

Fig. 7 Mean tilt angle ϕ *versus* channel width d/A for different amplitudes A/λ at $\lambda = 21a_0$ and $\nu = 0.003/\tau_0$. Inset: Maximum tilt angle ϕ_{max} *versus* $(A/\lambda)^2$. The dashed blue line is a linear fit to the data points.

In Fig. 8 we plot it *versus* the channel width d/A. Starting from $d/A \in [1,2]$, where the Taylor line squeezes into the channel, γ increases and goes through a maximum at $d/A \approx 3$. Interestingly, the maximum value of γ is approximately the same, only for the smallest amplitude the maximum is larger and shifted towards $d/A \approx 4$. As before, at $d/A \gtrsim 8$ the factor γ reaches a plateau value γ_∞. Obviously, this happens when the other channel wall does no longer influence the swimming Taylor line by hydrodynamic interactions. So the presence of both channel walls helps to speed up the Taylor line with an optimal channel width at $d/A \approx 3$.

The inset shows how γ_∞ decreases with increasing wave amplitude A and reaches nearly one at $A/\lambda = 0.24$. This suggests the following interpretation. The Taylor line uses the no-slip condition of the fluid at the channel wall to push itself forward.

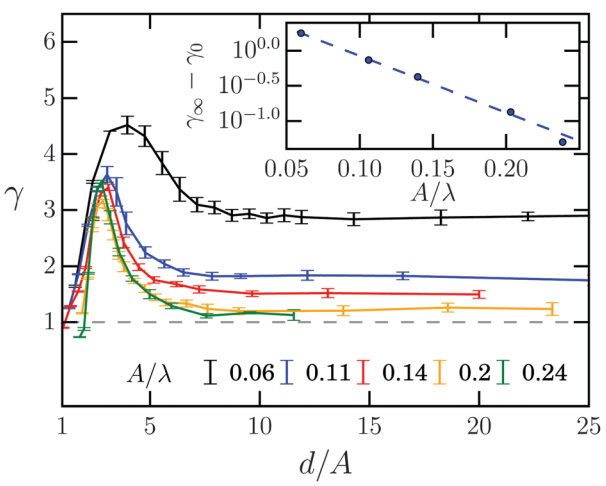

Fig. 8 Speed enhancement *versus* dimensionless channel width d/A for different amplitudes A/λ. The inset plots $\log(\gamma_\infty - \gamma_0)$ *versus* A/λ, where γ_∞ is the plateau value and γ_0 a fit parameter. The dashed line shows an exponential fit to $\gamma_\infty - \gamma_0 = \gamma_1 \exp(-\gamma_2 A/\lambda)$. Fit parameters are $\gamma_0 = 1.08 \pm 0.03$, $\gamma_1 = 5.4 \pm 0.3$, and $\gamma_2 = -18.6 \pm 0.9$.

This is more effective the closer the Taylor line swims at the wall, *i.e.*, for small A. In contrast, with increasing A also the mean distance of the Taylor line from the wall increases and one expects to reach the bulk value of the swimming speed ($\gamma_\infty = 1$) at large A. The dashed line in the inset is an exponential fit to $\gamma_\infty - \gamma_0 = \gamma_1 \exp(-\gamma_2 A/\lambda)$. We find that $\gamma_0 = 1.08$ deviates from the ideal large-amplitude value of one. This is due to a numerical artifact since for large A the MPCD fluid is no longer incompressible.[82]

V. Taylor line in a cubic obstacle lattice

We now study the Taylor line swimming in a cubic lattice of obstacles with lattice constant d. Fig. 9 shows the cubic unit cell. The obstacles have a diameter $2R/\lambda$, which we always refer to the wavelength $\lambda = 21a_0$ of the Taylor line. By varying d and R, the Taylor line enters different swimming regimes, which we will discuss in detail in what follows.

A. Dilute obstacle lattice

To define the dilute obstacle lattice, we introduce the width of the gap between two neighboring obstacles,

$$d_{surf} = d - 2R. \tag{17}$$

For $d_{surf} > 2A$ the Taylor line with amplitude A can freely swim through the gap, whereas for $d_{surf} < 2A$ it has to squeeze through the gap and therefore adjusts its swimming direction. This leads to what we call geometrical swimming, which we will discuss in the following section.

We illustrate the first case, $d_{surf} > 2A$, in Fig. 9, which shows the probability density $P(\vec{r})$ for all the beads of the Taylor line to visit a position $\vec{r}$ in the cubic unit cell. The probability density with the blue thin stripes shows that the Taylor line never

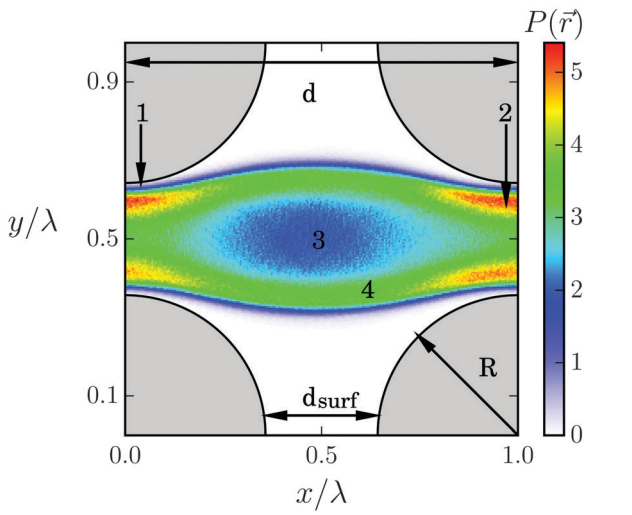

Fig. 9 Taylor line swimming in a dilute lattice of obstacles (gray quadrants). The color code shows the probability density $P(\vec{r})$ for all bead positions of the Taylor line in the cubic unit cell with lattice constant $d/\lambda = 1$, obstacle diameter $2R/\lambda = 0.714$, and gap width $d_{surf} = 2.04A$. The regions (1)–(4) are discussed in the main text.

This journal is © The Royal Society of Chemistry 2016

Open Access Article. Published on 15 July 2016. Downloaded on 1/23/2026 2:08:07 AM.
This article is licensed under a Creative Commons Attribution 3.0 Unported Licence.

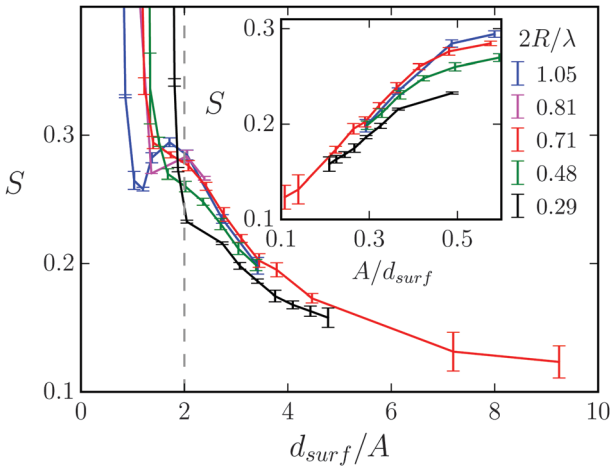

Fig. 10 Stroke efficiency S plotted *versus* gap width d_{surf} for different diameters of the obstacles with $\lambda = 21a_0$ and $A/\lambda = 0.14$. The vertical dashed line separates the region of dilute ($d_{surf} > 2A$) and dense ($d_{surf} < 2A$) obstacle lattices. Inset: S plotted *versus* $1/d_{surf}$.

leaves its lane. This is also true for other values of d/λ as long as the Taylor line cannot freely rotate in the space between the lattices. A closer inspection also shows a thin white region (1) around the obstacles, which the Taylor line never enters. Nevertheless, the probability of the beads for being in region (2) in the narrow gap between the obstacles is much higher than for being in region (3) between the four obstacles. We understand this as follows. The beads move up and down while moving with the Taylor line. In region (2) the beads reach their largest displacement equal to A and slow down to invert their velocity. So, they spend more time in region (2), which explains the high residence probability not only in (2) but also in region (4).

In Fig. 10 we plot the stroke efficiency as a function of d_{surf}/A for different $2R/\lambda$. For $d_{surf}/A > 2$ the stroke efficiency ultimately is proportional to $1/d_{surf}$ as the inset demonstrates. In addition, at constant d_{surf} the efficiency S is roughly the same, stronger deviations only occur at the smallest $2R/\lambda = 0.29$. This means S is mainly determined by the gap width, through which the Taylor line has to move when A is kept constant. For $d_{surf} < 2A$ the Taylor line has to squeeze through the obstacle lattice. In the main plot of Fig. 10 one realizes a transition in all the curves, where S increases sharply. As we discuss in Section V.B, this is where the swimming Taylor line fits perfectly along one of the lattice directions and geometric swimming takes place.

B. Geometric swimming in a dense obstacle lattice

In dense obstacle lattices ($d_{surf} < 2A$) a new swimming regime occurs when the lattice constant d is appropriately tuned. Starting to swim in the horizontal direction (see Movie M1 in the ESI†), the Taylor line adjusts its swimming direction along a lattice direction with lattice vector $\vec{g} = d(m\vec{e}_x + n\vec{e}_y)$, which defines the swimming mode (m,n). We call this regime geometrical swimming. Fig. 11 shows a few examples each with three snaphots of the Taylor line in green, red, and blue, where the time difference between the snapshots is between T and $2T$. Perfect geometrical swimming occurs when one wave train fits perfectly into the lattice meaning

$$\lambda = d_{\text{eff}} = d\sqrt{m^2 + n^2}, \tag{18}$$

where we have introduced the magnitude of the relevant lattice vector $d_{\text{eff}} = |\vec{g}|$. The (2,1) mode in the Movie M1 (ESI†) is a good example for geometric swimming. Depending on radius R and amplitude A, the Taylor line also pushes against the obstacles. Obviously, for perfect geometrical swimming the swimming velocity $v_{\parallel}$ and the phase velocity c have to be identical: $v_{\parallel} = c$. The Taylor line swims with an efficiency $S = 1$. It behaves like a corkscrew, which is twisted into a cork; after a full rotation the corkscrew has advanced by exactly one pitch. Differently speaking, the Taylor line converts the bending wave optimally into a net motion without any slip between the Taylor line and viscous fluid. However, geometrical swimming also occurs when the perfect swimming condition is only approximately fulfilled, $\lambda \approx d\sqrt{m^2 + n^2}$. In this case, the Taylor line pushes against the obstacles and the swimming velocity deviates from c but can even achieve values larger than c. We discuss this in the following. Note that several of these swimming modes, in particular the (1,1) mode, have been observed in experiments for *C. elegans* in an obstacle lattice.[52,53]

In the geometric swimming regime, the swimming efficiency $S = v_{\parallel}/c$ can be rewritten in pure geometric quantities. Using $v_{\parallel} = d_{\text{eff}}\nu$ and $c = \lambda\nu$, we immediately arrive at

$$S = \frac{v_{\parallel}}{c} = \frac{d_{\text{eff}}}{\lambda}. \tag{19}$$

In Fig. 12 we plot this relation as a dashed line together with the gray shaded region to indicate the geometric-swimming regime. The figure plots the stroke efficiency of a Taylor line swimming predominantly along the diagonal direction in the lattice as a function of d_{diag}, which is the diagonal distance of the obstacles. The curve parameter is the obstacle radius R/λ. The sharp increase of S in the orange curve ($2R/\lambda = 0.62$) at $d_{\text{diag}} = 0.9$ indicates a transition from a swimming mode, where the Taylor line has to squeeze through the obstacle lattice, to the geometric-swimming regime. Then, a sharp decrease in S follows and ultimately S decreases slowly. Increasing d_{diag} at constant R makes the gaps between the obstacles wider and at the sharp decrease the Taylor line enters the regime of dilute obstacle lattices discussed in the previous section.

The regime of geometric swimming extends over a finite interval in d_{diag}. One recognizes that geometric swimming can also be implemented when $d_{\text{diag}} = \lambda$ is not exactly fulfilled. Even swimming velocities larger than the wave velocity c ($S > 1$) are realized. Fig. 13 illustrates the mechanism for $d_{\text{diag}} > \lambda$. It shows the probability density $P(\vec{r})$ summed over all beads to occupy a position between the obstacles. $P(\vec{r})$ reveals two sliding tracks of the Taylor line. A closer inspection shows that the head ($nl_0 \in [0,0.2L_c]$) and middle ($nl_0 \in [0.2L_c,0.7L_c]$) sections move on the "pushing" track. When the bending wave passes along the Taylor line, the Taylor line pushes against the obstacles (indicated by the red arrows), which helps it to swim

Open Access Article. Published on 15 July 2016. Downloaded on 1/23/2026 2:08:07 AM.
This article is licensed under a Creative Commons Attribution 3.0 Unported Licence.

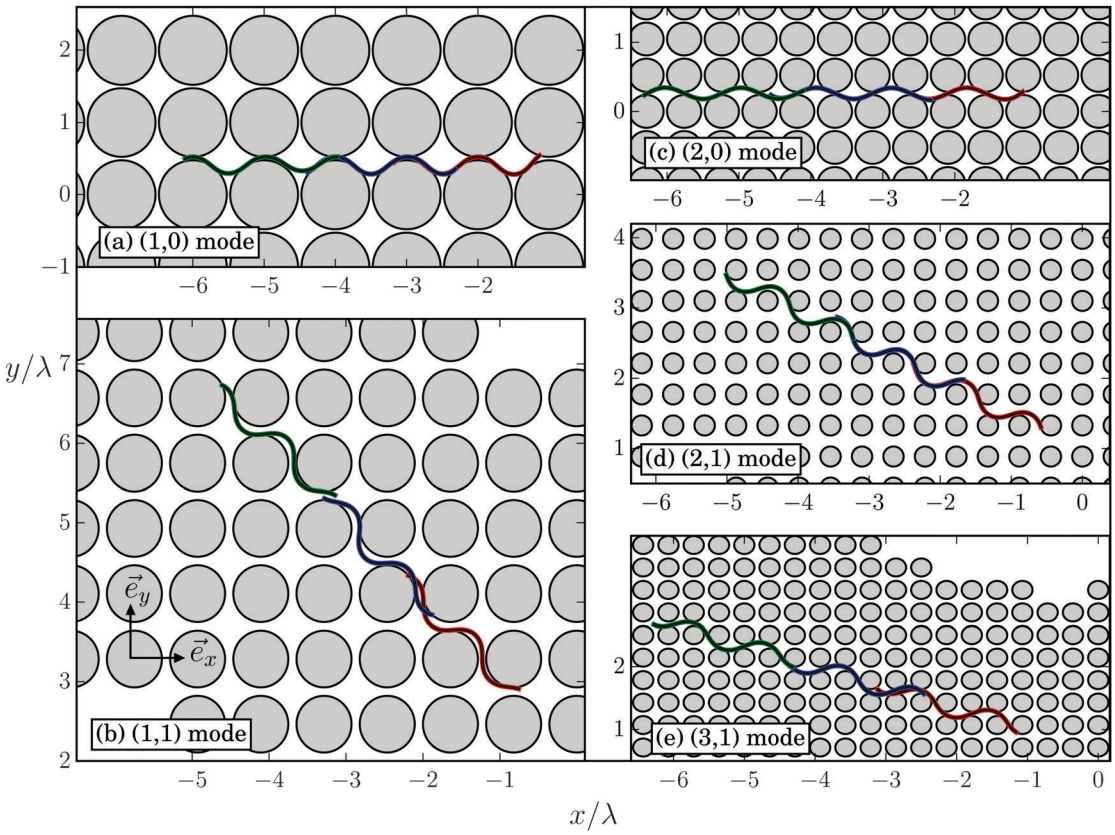

Fig. 11 Geometrical swimming of the Taylor line in a dense cubic lattice of obstacles (gray circles). Depending on the lattice constant d, the Taylor line swims in different lattice directions with mode index (m,n), where $d(m\vec{e}_x + n\vec{e}_y)$ gives the direction of one wave train of the Taylor line and $\lambda \approx d\sqrt{m^2+n^2}$. Three snapshots with a time difference between T and $2T$ are shown. The parameters of the illustrated swimming modes are: (a) (1,0) mode with $d/\lambda = 0.95$ and $2R/\lambda = 0.95$, (b) (1,1) mode with $d_{diag}/\lambda = 1.08$ and $2R/\lambda = 0.71$, (c) (2,0) mode with $d/\lambda = 0.52$ and $2R/\lambda = 0.48$, (d) (2,1) mode with $d/\lambda = 0.44$ and $2R/\lambda = 0.29$ [note $(2^2 + 1^2)^{-0.5} \approx 0.45$], (e) (3,1) mode with $d/\lambda = 0.35$ and $2R/\lambda = 0.29$ [note $(3^2 + 1^2)^{-0.5} \approx 0.31$].

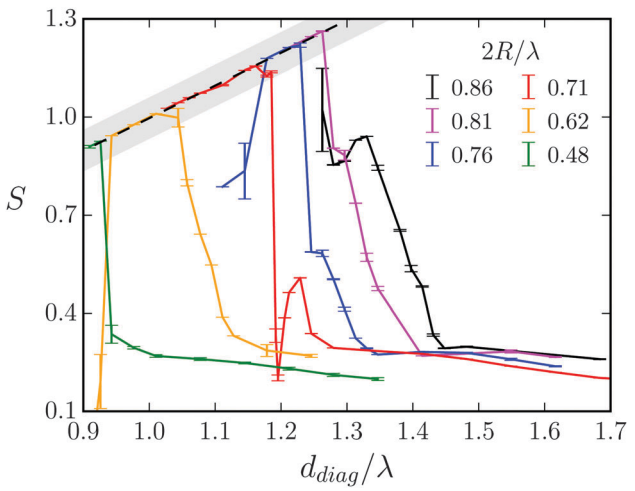

Fig. 12 The stroke efficiency $S = v_{||}/c$ for a Taylor line swimming predominantly in the diagonal direction, *i.e.*, in the (1,1) mode. S is plotted *versus* the diagonal distance d_{diag}/λ between two obstacles for different obstacle diameters $2R/\lambda$. The gray shaded area shows the geometrical swimming regime and the dashed line with slope one indicates the geometric-swimming relation $S = d_{diag}/\lambda$ from eqn (19).

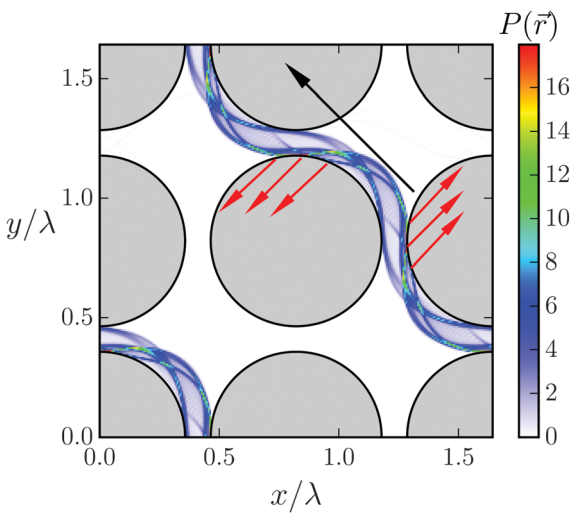

Fig. 13 Probability density $P(\vec{r})$ for all beads to visit a position in four unit cells during geometrical swimming. The parameters are $d_{diag}/\lambda = 1.16$ and $2R/\lambda = 0.714$. The black arrow shows the swimming direction and the red arrows indicate where the head and the middle section of the Taylor line push against the obstacles.

This journal is © The Royal Society of Chemistry 2016

Open Access Article. Published on 15 July 2016. Downloaded on 1/23/2026 2:08:07 AM.
This article is licensed under a Creative Commons Attribution 3.0 Unported Licence.

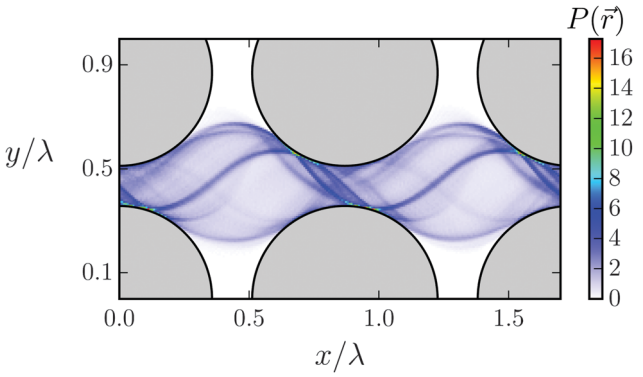

Fig. 14 Probability density $P(\vec{r})$ for all beads of the Taylor line to visit a position between the obstacles. The Taylor line pushes against the obstacles. The parameters are $d_{diag}/\lambda = 1.23$ or $d/\lambda = 0.87$, $2R/\lambda = 0.714$, and $d_{surf}/A = 1.11$.

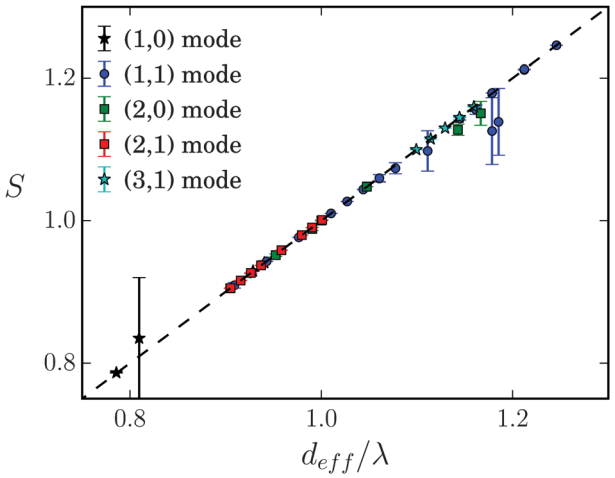

Fig. 15 Stroke efficiency S *versus* effective distance d_{eff}/λ defined in eqn (18) for different swimming modes (m,n) and for different parameters. All data in the geometrical swimming regime collapse on one master curve.

faster than in the ideal case. This is nicely illustrated in Movie M1 in the ESI† for the (1,1) mode. The other track is mainly occupied by the tail section ($nl_0 \in [0.7L_c, L_c]$) which does not contribute to the increased propulsion. In between the tracks there is a blurry area indicating that the part of the Taylor line between the middle and tail section has to transit from the pushing to the other track.

At larger obstacle diameters in Fig. 12 (red, blue, and purple line) the sharp decrease in S after the geometric swimming indicates a different transition. The Taylor line changes the direction and swims along the (1,0) direction since then the wavelength λ fits better to the spatial period, $\lambda \approx d$. The local maximum in the red curve develops into a shoulder, which for the purple curve belongs to the (1,0) mode of geometrical swimming. Finally, for the black line ($2R/\lambda = 0.86$) geometric swimming along the (1,0) direction is more developed. In Fig. 14 we show the positional probability density of all beads of the Taylor line exactly at the local maximum of the red curve in Fig. 12. With $d/\lambda = 0.87$ the Taylor line is not in the geometric swimming regime. Even though the distribution is much more blurred than before, there is still a clear sinusoidal track visible. The Taylor line pushes against the obstacles, which helps it to move through the narrow gap. Finally, the red curve in Fig. 12 becomes flat when the Taylor line enters the dilute-lattice regime.

For lattice constants d well below λ and smaller obstacle diameters $2R$, one also observes the higher modes (2,0), (2,1), and (3,1) visualized in Fig. 11. In Fig. 15 we summarize all our results by plotting S for the different swimming modes against the specific d_{eff} defined in eqn (18). The resulting master curve impressively illustrates the significance of geometrical swimming even reaching swimming velocities up to 20% larger than the ideal value from the phase velocity c. Thus, swimming in an obstacle lattice results in a new type of swimming compared to conventional locomotion at small Reynolds numbers, it resembles rather a corkscrew twisted into cork.

C. More complex trajectories

In Fig. 16 we show examples of trajectories that do not show geometric swimming along a defined direction as discussed in Section V.B but exhibit more complex shapes. They are also nicely illustrated in Movie M2 of the ESI.† Depending on the specific values for lattice constant d/λ and obstacle diameter $2R/\lambda$, we can identify trajectories of different types. They either define new swimming modes [Fig. 16(a), (c) and (d)] or combine two geometric-swimming modes [Fig. 16(b)]. In Fig. 16(a) the obstacle lattice is so dense that the Taylor line cannot develop geometric swimming. Instead, it swims alternatively along the horizontal and vertical directions for four or two lattice constants, respectively, which results in a trajectory of rectangular shape. Fig. 16(b) shows the Taylor line while it switches its running mode between the (1,1) and (3,1) swimming directions (see also Movie M2, ESI†).

A new trajectory type occurs when both the obstacle diameter $2R/\lambda$ and the lattice constant d/λ roughly agree with the wavelength (see also Movie M2, ESI†). In this case, after some transient regime the Taylor line is trapped and swims around a square of the same four obstacles [trapped circle mode in Fig. 16(c)] or around a single obstacle [trapped circle mode in Fig. 16(d)].

D. Variation of the length of the Taylor line

In Fig. 17 we plot the stroke efficiency S *versus* diagonal obstacle distance d_{diag} for different lengths L/λ of the Taylor line. We keep the wavelength and the obstacle radius constant. For $L/\lambda = 0.5$ the Taylor line hardly swims persistently, neither when it is strongly confined by the obstacles ($d_{diag}/\lambda < 1.3$) nor when it does not touch the obstacles at all ($d_{diag}/\lambda > 1.3$). This is nicely illustrated in Movie M3 (ESI†). For $L/\lambda = 2$ and 3 the Taylor lines first are clearly in the geometric-swimming regime along the (1,1) direction. The strong decrease of S at around $d_{diag}/\lambda = 1.2$ indicates the transition to swimming along the (1,0) direction. Right at the deep minimum of the red curve ($L/\lambda = 2$) the Taylor line gets more or less stuck before it enters the (1,0) swimming direction. At *ca.* $d_{diag}/\lambda > 1.4$ the obstacles

Open Access Article. Published on 15 July 2016. Downloaded on 1/23/2026 2:08:07 AM.
This article is licensed under a Creative Commons Attribution 3.0 Unported Licence.

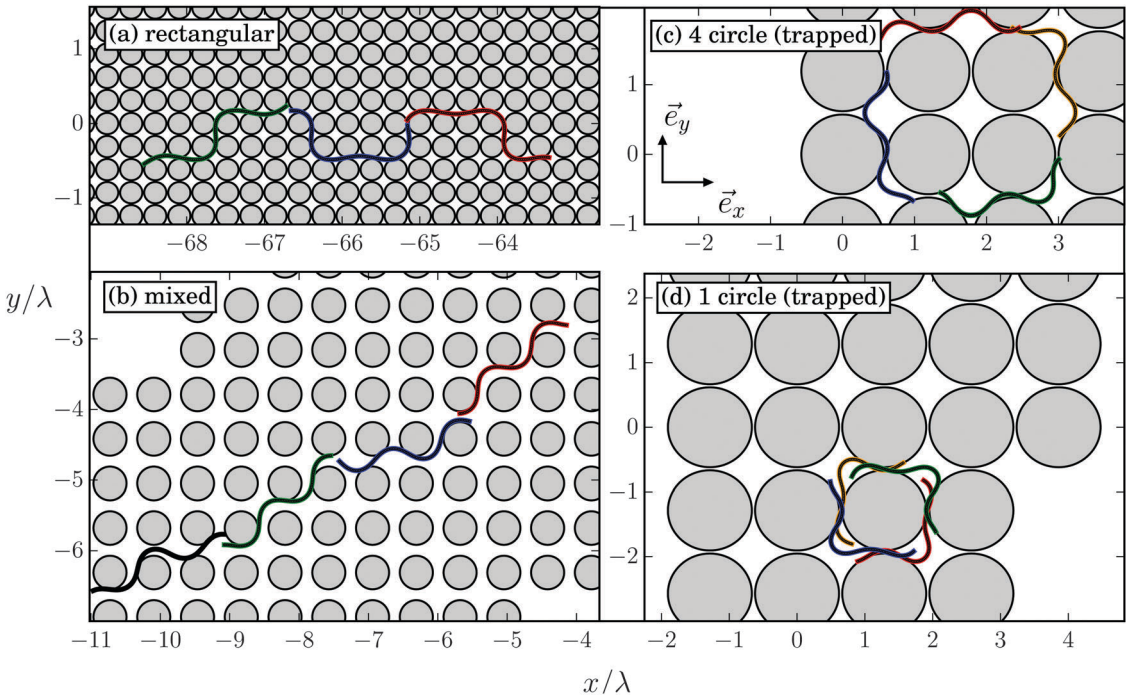

Fig. 16 In a dense obstacle lattice more complex trajectories occur at specific values of lattice constant d/λ and obstacle diameter $2R/\lambda$. Several snapshots of the Taylor line are shown: (a) rectangular mode at d/λ = 0.31 and $2R/\lambda$ = 0.29; (b) mixed mode at d/λ = 0.63 and $2R/\lambda$ = 0.48, where the Taylor line switches between the (1,1) and (3,1) swimming direction; (c) 4 circle (trapped) mode at d/λ = 1.19 and $2R/\lambda$ = 1.14, where the Taylor line circles around four obstacles; and (d) 1 circle (trapped) mode at d/λ = 1.29 and $2R/\lambda$ = 1.24, where it circles around one obstacle after an initial transient regime.

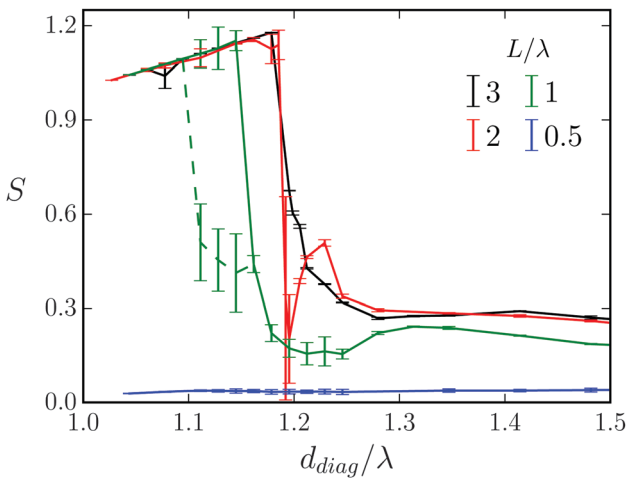

Fig. 17 Stroke efficiency S *versus* diagonal distance d_{diag}/λ for different lengths L/λ of the Taylor line at wavelength $\lambda = 21a_0$ and obstacle radius R/λ = 0.71.

are sufficiently apart from each other and the Taylor line does not push against them anymore.

At length $L/\lambda = 1$ and *ca.* $d_{diag}/\lambda = 1.1$ a new feature occurs. The Taylor line switches between geometric swimming along the (1,1) and (1,0) directions. This is illustrated by the two branches of the green curve in Fig. 17 and in Movie M4 (ESI†) for $d_{diag}/\lambda = 1.13$. In the following broad minimum of the green curve ($1.17 < d_{diag}/\lambda < 1.25$), the Taylor line exhibits some stick-slip motion. It first pushes frequently against one obstacle and then swims more or less continuously for one lattice constant (see Movie M4, ESI† for $d_{diag}/\lambda = 1.2$). Again, at $d_{diag}/\lambda > 1.4$ the Taylor line does not push anymore against the obstacles while swimming.

VI. Summary and conclusions

We have implemented an undulatory Taylor line in a Newtonian fluid using the method of multi-particle collision dynamics and a sinusoidal bending wave running along the Taylor line. We have calibrated the parameters such that its persistence length is much larger than the contour length in order to observe regular undulatory shape changes and directed swimming.

In microchannels the Taylor line swims to one channel wall. Swimming speed is enhanced due to hydrodynamic interactions and the Taylor line is oriented with an acute tilt angle at the wall similar to simulations of sperm cells.[38] The acute angle can be understood by monitoring the initiated flow fields. In wide channels the tilt angle increases quadratically with the amplitude A of the bending wave, while the speed enhancement decreases exponentially with increasing A since the Taylor line swims, on average, further away from the wall. In narrow channels the swimming speed has a maximum at roughly $d/A \approx 3$. The Taylor line uses the no-slip condition of the fluid at the walls to effectively push itself forward.

 This journal is © The Royal Society of Chemistry 2016

Open Access Article. Published on 15 July 2016. Downloaded on 1/23/2026 2:08:07 AM.
This article is licensed under a Creative Commons Attribution 3.0 Unported Licence.

In a dilute obstacle lattice swimming speed is also enhanced due to hydrodynamic interactions with the obstacles. In the dense obstacle lattice we could reproduce the geometrical swimming observed in the case of *C. elegans*[52,53] even though we did not consider any finite extension of the Taylor line. In addition, we found more complex swimming modes, which occur due to the strong confinement between the obstacles. In the geometrical swimming regime the Taylor line strongly interacts with the obstacles and swims with a speed close to the phase velocity of the bending wave, thus much more efficiently than in a pure bulk fluid. Geometrical swimming occurs when the wavelength of the Taylor line fits into the lattice along one specific direction. Thus, the swimming efficiencies of various geometrical swimming modes, plotted *versus* the ratio d_{eff}/λ of the effective obstacle distance and undulation wavelength, all collapse on the same master curve. Increasing d_{eff}/λ beyond one, even swimming speeds larger than the phase velocity of the bending wave occur but ultimately the Taylor line enters a different swimming mode. Thus, one can control the swimming direction of undulatory microorganisms by tuning the lattice constant of an obstacle lattice. This might be used for a microfluidic sorting device.

The concept of geometrical swimming goes back to Berg and Turner in order to explain the enhanced swimming of helical bacteria in polymer networks of viscoelastic fluids.[48] Further studies on the undulatory Taylor line should investigate the enhanced swimming speed in more disordered obstacle suspensions and when the obstacles are allowed to move, which models more realistic environments such as blood. In both cases we expect the principle of geometric swimming to be applicable. However, the classification of a unique swimming mode with index (m,n), indicating the swimming direction, will no longer be possible. Instead, for fixed obstacles the Taylor line might switch between different modes, according to the local environment, but also become trapped while exploring possible swimming directions. All this will crucially depend on the size, polydispersity, and density of the obstacles. On sufficiently large length scales the swimmer then enters a diffusive motion. In a fluid with movable obstacles, the Taylor line is able to create a favorable environment by pushing the obstacles around. However, the swimming speed will be smaller than the ideal value given by the phase velocity c, since the movable obstacles give less resistance to the pushing Taylor line compared to fixed obstacles. All these considerations should be checked by further detailed simulations. By studying the principle of geometric swimming in the ideal case, this paper provides a guiding principle for understanding swimming in more complex environments.

Appendix A: calibration of parameters

We calibrate the amplitude A and wavelength λ of the Taylor line by varying the number of beads N and the curvature parameter b. The parameters used in this article are summarized in Table 1. The contour length is calculated using eqn (7).

Table 1 Calibration of the parameters of the Taylor line. The bead number N and curvature parameter b are the input parameters which determine wavelength λ and amplitude A. Lengths are given in units of the edge length a_0 of the collision cells

N	b	λ/a_0	A/a_0
88	0.105	21.02	1.26
94	0.168	21.02	2.23
97	0.18725	20.99	2.60
100	0.06	24.40	0.94
100	0.15	22.59	2.27
100	0.2	20.99	2.93
105	0.2162	20.98	3.43
125	0.24	21.04	5.02

Acknowledgements

We acknowledge helpful discussions with C. Prohm, J. Blaschke, and A. Zöttl. This research was funded by grants from DFG through the research training group GRK 1558, project STA 352/9, and within the priority program SPP 1726 'Microswimmers – from Single Particle Motion to Collective Behaviour' (STA 352/11).

References

1 E. Lauga and T. R. Powers, *Rep. Prog. Phys.*, 2009, **72**, 096601.
2 E. M. Purcell, *Am. J. Phys.*, 1977, **45**, 3.
3 J. Lighthill, *SIAM Rev.*, 1976, **18**, 161.
4 S. Suarez and A. A. Pacey, *Hum. Reprod. Update*, 2006, **12**, 23.
5 I. R. Gibbons, *J. Cell Biol.*, 1981, **91**, 107s.
6 H. C. Berg, *Bacterial motility: handedness and symmetry*, John Wiley & Sons, Ltd, 1991, pp. 58–72.
7 H. C. Berg, *E. coli in Motion*, Springer Science & Business Media, 2008.
8 R. Vogel and H. Stark, *Phys. Rev. Lett.*, 2013, **110**, 158104.
9 T. C. Adhyapak and H. Stark, *Phys. Rev. E: Stat., Nonlinear, Soft Matter Phys.*, 2015, **92**, 052701.
10 J. Hu, M. Yang, G. Gompper and R. G. Winkler, *Soft Matter*, 2015, **11**, 7867.
11 N. Heddergott, T. Krueger, S. Babu, A. Wei, E. Stellamanns, S. Uppaluri, T. Pfohl, H. Stark and M. Engstler, *PLoS Pathog.*, 2012, **8**, e1003023.
12 R. S. Berman, O. Kenneth, J. Sznitman and A. M. Leshansky, *New J. Phys.*, 2013, **15**, 075022.
13 A. Bilbao, E. Wajnryb, S. A. Vanapalli and J. Blawzdziewicz, *Phys. Fluids*, 2013, **25**, 081902.
14 G. Taylor, *J. R. Soc., Interface*, 1951, **209**, 447.
15 G. Taylor, *Proc. R. Soc. A*, 1959, **253**, 313.
16 G. J. Elfring and E. Lauga, *Phys. Rev. Lett.*, 2009, **103**, 088101.
17 T. D. Montenegro-Johnson and E. Lauga, *Phys. Rev. E: Stat., Nonlinear, Soft Matter Phys.*, 2014, **89**, 060701.
18 R. Dreyfus, J. Baudry and H. Stone, *Eur. Phys. J. B*, 2005, **47**, 161.
19 E. Gauger and H. Stark, *Phys. Rev. E: Stat., Nonlinear, Soft Matter Phys.*, 2006, **74**, 021907.
20 R. Zargar, A. Najafi and M. Miri, *Phys. Rev. E: Stat., Nonlinear, Soft Matter Phys.*, 2009, **80**, 026308.

Open Access Article. Published on 15 July 2016. Downloaded on 1/23/2026 2:08:07 AM.
This article is licensed under a Creative Commons Attribution 3.0 Unported Licence.

21 D. Crowdy, *Int. J. Non Linear Mech.*, 2011, **46**, 577.
22 L. Rothschild, *Nature*, 1963, **198**, 1221.
23 A. P. Berke, L. Turner, H. C. Berg and E. Lauga, *Phys. Rev. Lett.*, 2008, **101**, 038102.
24 Y. Or and R. M. Murray, *Phys. Rev. E: Stat., Nonlinear, Soft Matter Phys.*, 2009, **79**, 045302.
25 J. Elgeti and G. Gompper, *Europhys. Lett.*, 2009, **85**, 38002.
26 G. Li and J. X. Tang, *Phys. Rev. Lett.*, 2009, **103**, 078101.
27 G. Li, J. Bensson, L. Nisimova, D. Munger, P. Mahautmr, J. X. Tang, M. R. Maxey and Y. V. Brun, *Phys. Rev. E: Stat., Nonlinear, Soft Matter Phys.*, 2011, **84**, 041932.
28 K. Obuse and J.-L. Thiffeault, in *Natural Locomotion in Fluids and on Surfaces*, ed. S. Childress, A. Hosoi, W. W. Schultz and J. Wang, The IMA Volumes in Mathematics and its Applications, Springer, New York, 2012, vol. 155, pp. 197–206.
29 A. Zöttl and H. Stark, *Phys. Rev. Lett.*, 2012, **108**, 218104.
30 A. Zöttl and H. Stark, *Eur. Phys. J. E: Soft Matter Biol. Phys.*, 2013, **36**, 4.
31 J. Elgeti and G. Gompper, *Europhys. Lett.*, 2013, **101**, 48003.
32 G.-J. Li and A. M. Ardekani, *Phys. Rev. E: Stat., Nonlinear, Soft Matter Phys.*, 2014, **90**, 013010.
33 S. E. Spagnolie and E. Lauga, *J. Fluid Mech.*, 2012, **700**, 105.
34 S. Uppaluri, N. Heddergott, E. Stellamanns, S. Herminghaus, A. Zoettl, H. Stark, M. Engstler and T. Pfohl, *Biophys. J.*, 2012, **103**, 1162.
35 R. Rusconi, J. S. Guasto and R. Stocker, *Nat. Phys.*, 2014, **10**, 212.
36 E. Lauga, W. R. DiLuzio, G. M. Whitesides and H. A. Stone, *Biophys. J.*, 2015, **90**, 400.
37 M. d. C. Lopez-Garcia, R. L. Monson, K. Haubert, M. B. Wheeler and D. J. Beebe, *Biomed. Microdevices*, 2008, **10**, 709.
38 J. Elgeti, U. B. Kaupp and G. Gompper, *Biophys. J.*, 2010, **99**, 1018.
39 P. Denissenko, V. Kantsler, D. J. Smith and J. Kirkman-Brown, *Proc. Natl. Acad. Sci. U. S. A.*, 2012, **109**, 8007.
40 V. Kantsler, J. Dunkel and R. E. Goldstein, *Biophys. J.*, 2014, **106**, 210a.
41 K. Schaar, A. Zöttl and H. Stark, *Phys. Rev. Lett.*, 2015, **115**, 038101.
42 R. Nosrati, A. Driouchi, C. M. Yip and D. Sinton, *Nat. Commun.*, 2015, **6**, 8703.
43 Y. Yang, J. Elgeti and G. Gompper, *Phys. Rev. E: Stat., Nonlinear, Soft Matter Phys.*, 2008, **78**, 061903.
44 M. M. Mota, G. Pradel, J. P. Vanderberg, J. C. R. Hafalla, U. Frevert, R. S. Nussenzweig, V. Nussenzweig and A. Rodríguez, *Science*, 2001, **291**, 141.
45 J. P. Vanderberg and U. Frevert, *Int. J. Parasitol.*, 2004, **34**, 991.
46 M. Engstler, T. Pfohl, S. Herminghaus, M. Boshart, G. Wiegertjes, N. Heddergott and P. Overath, *Cell*, 2007, **131**, 505.
47 W. R. Schneider and R. N. Doetsch, *J. Bacteriol.*, 1974, **117**, 696.
48 H. C. Berg and L. Turner, *Nature*, 1979, **278**, 349.
49 X. N. Shen and P. E. Arratia, *Phys. Rev. Lett.*, 2011, **106**, 208101.
50 B. Liu, R. T. Powers and K. S. Breuer, *Proc. Natl. Acad. Sci. U. S. A.*, 2011, **108**, 19516.
51 V. A. Martinez, J. Schwarz-Linek, M. Reufer, L. G. Wilson, A. N. Morozov and W. C. K. Poon, *Proc. Natl. Acad. Sci. U. S. A.*, 2014, **111**, 17771.
52 S. Park, H. Hwang, N. Seong-Won, F. Martinez, R. H. Austin and W. S. Ryu, *PLoS One*, 2008, **3**, e2550.
53 T. Majmudar, E. E. Keaveny, J. Zhang and M. J. Shelley, *J. R. Soc., Interface*, 2012, **9**, 1809.
54 J. A. Voynow and B. K. Rubin, *Chest*, 2009, **135**, 505.
55 M. E. V. Johansson, J. K. Gustafsson, K. E. Sjöberg, J. Petersson, L. Holm, H. Sjövall and G. C. Hansson, *PLoS One*, 2010, **5**, e12238.
56 G. C. Hansson, *Curr. Opin. Microbiol.*, 2012, **15**, 57.
57 X. Druart, *Reprod. Domest. Anim.*, 2012, **47**, 348.
58 J. Teran, L. Fauci and M. Shelley, *Phys. Rev. Lett.*, 2010, **104**, 038101.
59 E. E. Riley and E. Lauga, *Europhys. Lett.*, 2014, **108**, 34003.
60 E. Lauga, *Phys. Fluids*, 2007, **19**, 083104.
61 H. C. Fu, T. R. Powers and C. W. Wolgemuth, *Phys. Rev. Lett.*, 2007, **99**, 258101.
62 H. C. Fu, C. W. Wolgemuth and T. R. Powers, *Phys. Fluids*, 2009, **21**, 033102.
63 G. Juarez, K. Lu, J. Sznitman and P. E. Arratia, *Europhys. Lett.*, 2010, **92**, 44002.
64 S. Babu, C. Schmeltzer and H. Stark, *Swimming at low Reynolds number: from sheets to African trypanosome*, Notes on Numerical Fluid Mechanics and Multidisciplinary Design, Springer, Berlin Heidelberg, 2012, vol. 119, pp. 25–41.
65 S. Babu and H. Stark, *New J. Phys.*, 2012, **14**, 085012.
66 D. Alizadehrad, T. Krueger, M. Engstler and H. Stark, *PLoS Comput. Biol.*, 2015, **11**, e1003967.
67 R. E. Wells and E. W. Merrill, *J. Clin. Invest.*, 1962, **41**, 1591.
68 P. W. Rand, E. Lacombe, H. E. Hunt and W. H. Austin, *J. Appl. Physiol.*, 1964, **19**, 117.
69 S. Jung, *Phys. Fluids*, 2010, **22**, 031903.
70 A. Battista, F. Frischknecht and U. S. Schwarz, *Phys. Rev. E: Stat., Nonlinear, Soft Matter Phys.*, 2014, **90**, 042720.
71 S. Johari, V. Nock, M. M. Alkaisi and W. Wang, *Lab Chip*, 2013, **13**, 1699.
72 S. H. Holm, J. P. Beech, M. P. Barrett and J. O. Tegenfeldt, *Lab Chip*, 2011, **11**, 1326.
73 G. Gompper, T. Ihle, D. Kroll and R. Winkler, *Adv. Polym. Sci.*, 2009, **221**, 1–87.
74 A. M. Leshansky, *Phys. Rev. E: Stat., Nonlinear, Soft Matter Phys.*, 2009, **80**, 051911.
75 A. Malevanets and R. Kapral, *J. Chem. Phys.*, 2000, **112**, 7260.
76 A. Malevanets and R. Kapral, *J. Chem. Phys.*, 1999, **110**, 8605.
77 H. Noguchi and G. Gompper, *Phys. Rev. E: Stat., Nonlinear, Soft Matter Phys.*, 2008, **78**, 016706.
78 R. Kapral, *Adv. Chem. Phys.*, 2008, **140**, 89–146.
79 E. Allahyarov and G. Gompper, *Phys. Rev. E: Stat., Nonlinear, Soft Matter Phys.*, 2002, **66**, 036702.
80 D. S. Bolintineanu, J. Lechman, S. J. Plimpton and G. S. Grest, *Phys. Rev. E: Stat., Nonlinear, Soft Matter Phys.*, 2012, **86**, 066703.

 This journal is © The Royal Society of Chemistry 2016

81 A. Lamura and G. Gompper, *Eur. Phys. J. E: Soft Matter Biol. Phys.*, 2001, **9**, 477.
82 J. T. Padding and A. A. Louis, *Phys. Rev. E: Stat., Nonlinear, Soft Matter Phys.*, 2006, **74**, 031402.
83 D. A. P. Reid, H. Hildenbrandt, J. T. Padding and C. K. Hemelrijk, *Phys. Rev. E: Stat., Nonlinear, Soft Matter Phys.*, 2012, **85**, 021901.
84 M. Peltomaki and G. Gompper, *Soft Matter*, 2013, **9**, 8346.
85 P. Kanehl and H. Stark, *J. Chem. Phys.*, 2015, **142**, 214901.
86 T. Ihle and D. M. Kroll, *Phys. Rev. E: Stat., Nonlinear, Soft Matter Phys.*, 2001, **63**, 020201.
87 T. Ihle and D. M. Kroll, *Phys. Rev. E: Stat., Nonlinear, Soft Matter Phys.*, 2003, **67**, 066705.
88 A. Zöttl and H. Stark, *Phys. Rev. Lett.*, 2014, **112**, 118101.
89 J. T. Padding, A. Wysocki, H. Löwen and A. A. Louis, *J. Phys.: Condens. Matter*, 2005, **17**, S3393.
90 P. Nelson, *Biological Physics*, W.H. Freeman and Company, 2008.

Open Access Article. Published on 15 July 2016. Downloaded on 1/23/2026 2:08:07 AM.
This article is licensed under a Creative Commons Attribution 3.0 Unported Licence.